Hybrid sensible-latent heat thermal energy storage using natural stones to enhance heat transfer: energy, exergy, and economic analysis

*Shuai Zhang, Ying Li, Yuying Yan**

Faculty of Engineering, University of Nottingham, University Park, Nottingham, UK
* Corresponding author, E-mail: Yuying.Yan@nottingham.ac.uk

ABSTRACT

Latent heat thermal energy storage addresses the mismatch between energy supply and demand; however, phase change materials (PCM) commonly have the issue of low thermal conductivity. Natural stones, as low-cost and environmentally friendly sensible heat storage media, are used to enhance the heat transfer of the PCM in the current study. Different stone types, sizes, and filling heights are tested, and a comprehensive energy, exergy, and economic analysis is performed. Results indicate that granite has the best heat transfer enhancement performance owing to superior thermal diffusivity, which accelerates the melting by 108% (initial temperature: 23 °C; heating temperature: 75 °C). Basalt with high specific heat contributes to the large energy capacity. The total exergy is hardly influenced by the stone size ranging from 15 mm to 40 mm, where the minimum is only 5.1% lower than the maximum. The exergy storage rate benefits from stones surrounding the inner tube and is increased by 246% with a filling height of 112.0 mm. The 40 mm-sized stones are the most cost-effective in the current testing conditions, and a 560% increase in the economy is achieved. This study demonstrates a high-performance, low-cost, environmentally friendly energy storage configuration and provides comprehensive information for potential energy recovery applications.

Keywords: natural stone; heat transfer enhancement; phase change material; energy analysis

1. Introduction

Thermal energy storage (TES) addresses the mismatch between energy supply and demand, both temporally and spatially. This characteristic makes TES an important method for energy recovery [1-4]. Generally, the TES is classified into sensible heat thermal energy storage (SHTES), latent heat thermal energy storage (LHTES), and thermochemical reaction thermal energy storage (TRTES) [5]. The TRTES is at the preliminary research stage of the laboratory, and there is a long way to practical applications [6].

Natural stones, as sensible heat storage media in SHTES, are widely accessible, low-cost, and environmentally friendly [7]. Their performance has been extensively investigated. Singh et al. [8] constructed a packed bed heat storage tank filled with 50 mm-diameter pebbles and studied the thermal performance under different conditions. The solar collection efficiency of the heat storage tank can reach 51%, and the heat release efficiency is around 75%. In Lugolole et al.'s research [9], where granite with diameters of 10.5 mm and 31.9 mm was used to store sensible heat energy, big stones were found to have a greater exergy rate than small ones. Audi [10] tested various stones for solar space heating and found that the storage volume required for a 50 m^2 collector was 8.9 m^3 when the storage medium was tarsand and 3.5 m^3 when the storage medium was zeolite. Tiskatine et al. [11] evaluated 52 types of stones as sensible heat storage materials for use in concentrating solar power plants. They considered multiple criteria, including compressive strength, density, thermal cycling resistance, thermal capacity, and thermal conductivity, and found that sandstone, gabbro, and dolerite were the best sensible heat storage media. Soprani et al. [12] tested different types of stones and studied the charging and discharging performance of a thermal energy storage tank. They focused on the influence of the buoyancy force on the temperature gradient and storage efficiency of a packed bed tank. Moreover, they analysed different charging powers, flow conditions, and bed configurations.

Phase change materials (PCM), the energy storage media in LHTES, are more attractive owing to the high energy storage density and the ability to maintain an almost constant temperature during charging/discharging [13, 14]. However, PCMs commonly have the issue of low thermal conductivity [15]. As Table S1 shows, the thermal conductivity of the PCM is much lower than that of the sensible heat storage materials (SHM), which leads to an unsatisfactory energy storage efficiency.

Several methods have been developed to enhance the heat transfer of the PCM, and a popular one is using porous skeletons such as metal foam and ceramic foam [16, 17]. Liu et al. [18] studied the charging process of the paraffin/copper foam composite in a horizontal shell-and-tube unit, and they analysed the influence of the structural characteristics on the storage performance. The total melting time is shortened by 300 s when the porosity decreases from 0.95 to 0.85, while it hardly changes with the pore size. Zhang and Yan [19] prepared ceramic foam used to enhance the heat transfer of molten salt. In addition, the authors conducted 200 heating/cooling cycles and tested the corrosion resistance to molten salt.

Fins are another widely used heat transfer enhancement structure. Yang et al. [20] performed a numerical investigation on the melting process of paraffin in a vertical shell-and-tube unit with annular fins. The effects of fin number, height, and thickness on the energy storage performance were analysed, and the complete melting time of paraffin can be shortened by 65%. Huang and Liu [21] designed tree-shaped fins to enhance the heat transfer of lauric acid and discussed the influence of the HTF direction. The numerical results indicate that the total melting and solidification time was shortened by 34.5% and 49.2%, respectively. The upward flow of the HTF is better for the melting process, while the downward flow is beneficial for the solidification process.

The third approach is adding highly conductive powders. Mahdi et al. [22] performed a numerical simulation and studied alumina nanoparticles in multi-PCMs. The heat storage unit

consisted of multiple segments which contained the PCM with a specific melting point each. Nanoparticles with a volume fraction of 5% can increase the solidification rate by 9.5%, 11%, and 19% for the one-PCM, two-PCM, and three-PCM, respectively. In Parsazadeh & Duan's research [23], adding nanoparticles led to a longer charging time and lower energy storage rate. In other words, using nanoparticles had a negative effect on energy storage, which is opposite to Mahdi et al.'s results [22].

The fourth method to address the low thermal conductivity of the PCM is using heat pipes. Shabgard et al. [24] reported a shell-and-tube heat storage unit with multiple heat pipes inserted between the HTF and PCM. They developed a thermal network model and quantified thermal performance using dimensionless heat pipe effectiveness. Nithyanandam and Pitchumani [25] analysed the effect of the number and orientation of heat pipes. Two modules were considered: for the first one, the PCM surrounded the inner tube through which the HTF flowed; for the second one, the PCM was contained within the inner tube over which the HTF flowed. The case with four heat pipes had superior effectiveness for both modules during charging and discharging.

Although various heat transfer enhancement methods have been investigated extensively, there are few studies on using natural stones to enhance the heat transfer of the PCM. Natural stones have much higher thermal conductivity than the PCM, as indicated in Table S1. In addition, they are widely accessible, and the cost is low. Moreover, they do not need additional material preparation and would not cause environmental issues. These advantages make natural stones promising thermal enhancers for the PCM. In previous studies, natural stones acted as sensible heat storage media for packed beds. In this research, they are used to enhance the heat transfer of the PCM for use in latent heat storage, which is the novelty of this research. In this study, different stone types, sizes, and filling heights are evaluated, and a comprehensive energy, exergy, and economic analysis is performed. Natural stones are combined with the PCM to

form a hybrid sensible-latent heat energy storage configuration, where stones not only act as sensible heat storage media but also as thermal enhancers. This study provides comprehensive information on the novel hybrid energy storage mode and guides the potential application in energy recovery.

2. Numerical model

2.1 System configuration

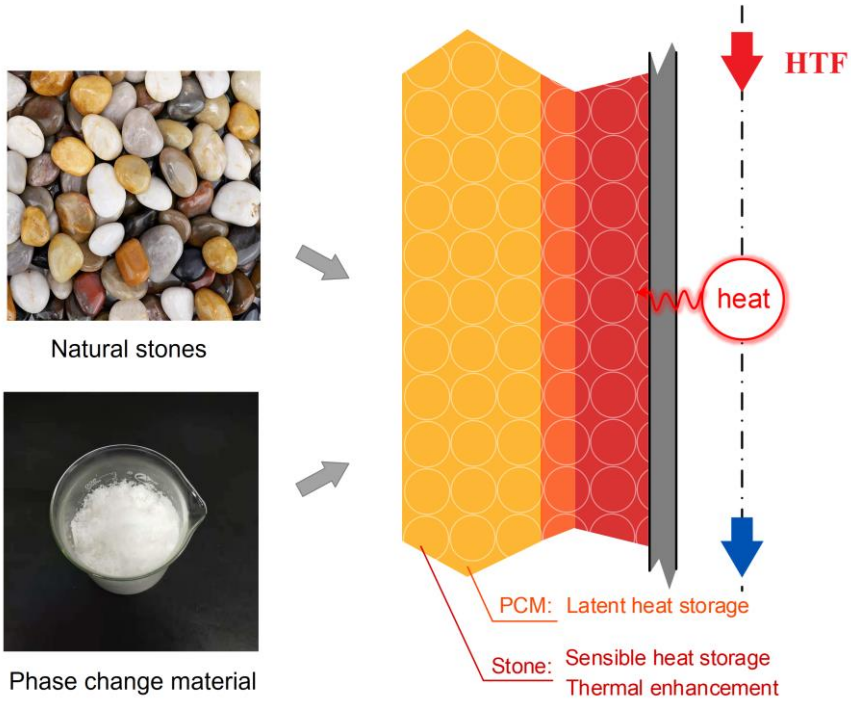

Figure 1. Schematic of the hybrid sensible-latent heat thermal energy storage configuration.

The schematic of the hybrid sensible-latent heat thermal energy storage configuration is shown in Figure 1, where the PCM and stones act as latent and sensible heat storage media, respectively; stones also serve as thermal enhancers of the PCM owing to high thermal conductivity (Table S1). In practice, the shape of natural stones is irregular, making it difficult to evaluate various factors like size, height, etc. Stones are assumed spherical to assess various factors and identify regularities.

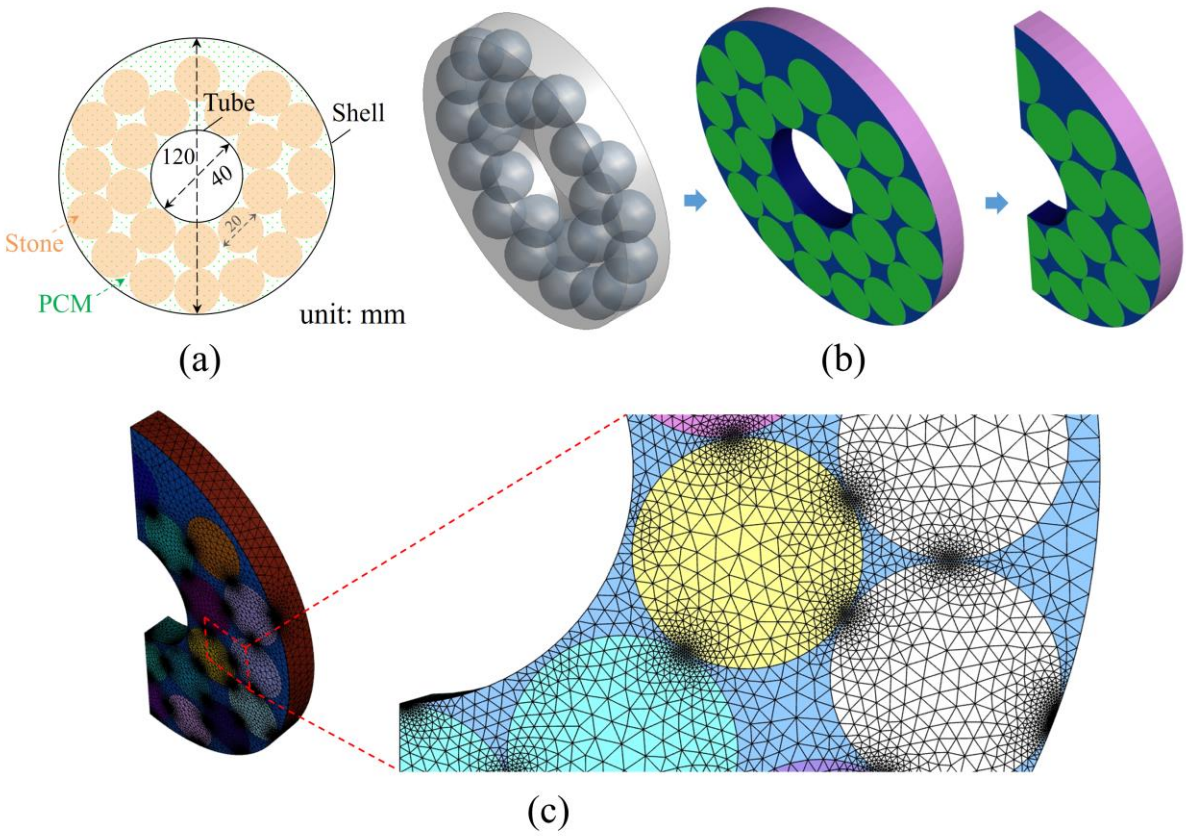

Figure 2. (a) Cross-section of the physical model; (b) schematic of the 3D physical model; (c) mesh of the computational domain.

Spherical stones are arranged tangent to each other in the shell-and-tube unit with an inner diameter of 40 mm and an outer diameter of 120 mm (Figure 2). In fact, there are several different arrangements of stones. The current arrangement considers gravity and makes the stones in contact with the tube as far as possible to conduct the tube's heat. The unit with one layer of stones was considered in the simulation, and only 1/4 unit was used as the final computational domain owing to symmetry (Figure 2(b)). The heating temperature of the tube is set as constant because the temperature of HTF hardly changes from the inlet to the outlet, as indicated in Figure S1. The shell is set as adiabatic [19].

The extremely small gap between two tangent spheres would lead to high skewness during meshing, which easily causes computational divergence. A solution is to reduce the size of the sphere to 0.99 times (the "near-miss" model) [26], which is adopted in the current study. The meshes between neighbouring spheres are refined, and the schematic of the surface meshes is

shown in Figure 2(c). The surface meshes are triangular; as the computational domain is a 3D structure, the volume meshes are generated based on these surface meshes, and they are polyhedral. The maximum skewness of the volume meshes is 0.78, which meets the requirement of the fluid simulation [27].

Six types of natural stones are considered: basalt, granite, gneiss, marble, quartzite, and sandstone. Their detailed properties are listed in Table 1. The filling height of stones is another factor influencing the energy storage performance, and five filling heights are included: 46.0 mm, 62.9 mm, 82.7 mm, 97.0 mm, and 112.0 mm. In addition, the impact of the size of stones is analysed: 15 mm, 20 mm, 25 mm, 30 mm, and 40 mm (diameter). The porosity of the simulated cases is presented in Table 2. Paraffin (RT60) is used as the PCM, and its properties are listed in Table 3. All the values are the same as those in Ref. [28] except for the viscosity, which is assumed to be 3.65 mPa·s in the current research. This research focuses on the low-temperature system because one of its potential applications is the in-place waste heat recovery with a temperature of several tens of degrees used for domestic hot water [29].

Table 1. Properties of natural stones [30, 31].

Type	Thermal conductivity, W/(m·K)	Density, kg/m^3	Specific heat, kJ/(kg·K)
Basalt	3.20	2,640	1.47
Granite	2.86	2,640	0.82
Gneiss	2.90	2,700	0.87
Marble	2.51	2,600	0.80
Quartzite	2.00	2,490	0.80
Sandstone	1.83	2,200	0.71

Table 2. Porosity of simulated cases.

Height, mm	Porosity, -	Size, mm	Porosity, -
46.0	0.83	15	0.55
62.9	0.75	20	0.52
82.7	0.67	25	0.61
97.0	0.58	30	0.63
112.0	0.52	40	0.50

Table 3. Thermo-physical properties of paraffin [28].

Property	Paraffin
Density, kg/m^3	785
Latent heat, J/kg	175,240
Melting point, °C	54.4–64.1
Specific heat, J/(kg·K)	2,850
Thermal conductivity, W/(m·K)	0.3 (solid)/0.1 (liquid)
Viscosity, mPa·s	3.65
Coefficient of thermal expansion, K^{-1}	3.085×10^{-4}

2.2 Governing equations

The following assumptions are made for the numerical simulation: (1) the PCM and stones are homogenous and isotropic; (2) the properties of energy storage materials, except for the density of the liquid PCM, are constant; (3) the liquid PCM is incompressible; (4) the Boussinesq approximation is adopted to deal with natural convection. Assumptions (1)-(4) are usually used in simulating the melting of the PCM and have been adopted in numerous studies such as Refs. [32-36]. The density of the liquid PCM is assumed to vary linearly with temperature in Boussinesq approximation; so, the natural-convection problem is simplified, and the convergence can be got faster [29, 37].

The enthalpy-porosity model is used to simulate the phase change of the PCM [38]. Instead of tracking the melt interface explicitly, this model calculates the liquid fraction in each cell

[39]. A cell is modelled as a "pseudo porous medium" where the porosity is equal to the liquid fraction. Namely, the porosity increases from 0 to 1 as the melting proceeds; 0 and 1 indicate the solid material and liquid material, respectively. In each cell, the liquid fraction and the porosity are uniform. The continuity equation of the liquid PCM is

$$\nabla \cdot \vec{U} = 0 \tag{1}$$

The momentum equations are:

$$\rho_{\mathrm{PCM}} \frac{\partial u}{\partial t} + \rho_{\mathrm{PCM}} \left(\vec{U} \cdot \nabla u \right) = - \frac{\partial p}{\partial x} + \mu_{\mathrm{PCM}} \nabla^2 u - \frac{(1-\varphi)^2}{(\varphi^3 + \omega)} A_{\mathrm{mushy}} u \tag{2}$$

$$\rho_{\mathrm{PCM}} \frac{\partial v}{\partial t} + \rho_{\mathrm{PCM}} \left(\vec{U} \cdot \nabla v \right) = - \frac{\partial p}{\partial y} + \mu_{\mathrm{PCM}} \nabla^2 v + \rho_{\mathrm{PCM}}\, g\, \beta (T - T_{\mathrm{m1}}) - \frac{(1-\varphi)^2}{(\varphi^3 + \omega)} A_{\mathrm{mushy}} v \tag{3}$$

$$\rho_{\mathrm{PCM}} \frac{\partial w}{\partial t} + \rho_{\mathrm{PCM}} \left(\vec{U} \cdot \nabla w \right) = - \frac{\partial p}{\partial z} + \mu_{\mathrm{PCM}} \nabla^2 w - \frac{(1-\varphi)^2}{(\varphi^3 + \omega)} A_{\mathrm{mushy}} w \tag{4}$$

where μ and β are the viscosity and the thermal expansion coefficient, respectively; A_{mushy} is the mushy zone constant (10^5); ω is a small number (0.001) to avoid being divided by zero. φ is the liquid fraction (the ratio of the liquid PCM volume to the total PCM volume) which is evaluated by [40]:

$$\varphi = \begin{cases} 0 & T < T_{\mathrm{m,\,l}} \\ \dfrac{T - T_{\mathrm{m,\,l}}}{T_{\mathrm{m,\,u}} - T_{\mathrm{m,\,l}}} & T_{\mathrm{m,\,l}} \le T \le T_{\mathrm{m,\,u}} \\ 1 & T > T_{\mathrm{m,\,u}} \end{cases} \tag{5}$$

where $T_{\mathrm{m,\,l}}$ and $T_{\mathrm{m,\,u}}$ are the lower and upper limits of the melting point of the PCM, respectively. The third term on the right side of Eq. (3) denotes the Boussinesq approximation considering the effect of the buoyancy force. The last terms in Eqs. (2)-(4) are the damping terms [41].

The energy equation of the PCM is given by [40]:

$$\rho_{\mathrm{PCM}}\, c_{\mathrm{p,\,PCM}} \left(\frac{\partial T}{\partial t} + \vec{U} \cdot \nabla T \right) = k_{\mathrm{PCM}} \nabla^2 T - \rho_{\mathrm{PCM}} L \frac{d\varphi}{dt} \tag{6}$$

where k, c_p and L are the thermal conductivity, specific heat, and latent heat, respectively.

Heat conduction takes place in the stones, and the energy equation is

$$\rho_{\text{stone}}\, c_{\text{p, stone}} \frac{\partial T}{\partial t} = k_{\text{stone}} \nabla^2 T \tag{7}$$

2.3 Initial/boundary conditions

The initial temperature of the whole computational domain is set as 23 °C, equal to the ambient temperature:

$$T_{\text{initial}} = 23°\text{C} \tag{8}$$

The heating temperate of the tube is set as 75 °C, higher than the liquidus temperature of PCM (64.1 °C):

$$T_{\text{tube}} = 75°\text{C} \tag{9}$$

The tube in this simulation is only 20 mm long at most, and the time for the HTF flowing from the inlet to the outlet is less than 0.5 s (flow rate: 4 L/min). It is hard to exert an effect on the cross-sectional temperature of the HTF within such a short time. Moreover, forced convection occurs in the HTF tube, which promotes the mixing of fluids and weakens the temperature difference. Thus, the isothermal heating boundary used in this simulation should be reasonable.

The shell is assumed adiabatic:

$$\frac{\partial T_{\text{shell}}}{\partial x} = 0, \quad \frac{\partial T_{\text{shell}}}{\partial y} = 0, \quad \frac{\partial T_{\text{shell}}}{\partial z} = 0 \tag{10}$$

The boundary between the PCM and stones is coupled. Namely, they have the same temperature at the boundary:

$$T_{\text{PCM}} = T_{\text{stone}} \tag{11}$$

and the same heat flux:

$$(-k_{\text{PCM}}\, \nabla T_{\text{PCM}}) \cdot \boldsymbol{n} = (-k_{\text{stone}}\, \nabla T_{\text{stone}}) \cdot \boldsymbol{n} \tag{12}$$

2.4 Grid and time step independence tests

The numerical model is solved using ANSYS Fluent. The governing equations are discretised using the finite volume method (FVM) and solved simultaneously. The pressure and velocity are coupled using the SIMPLE scheme, and the pressure, momentum, and energy terms are discretised using the second-order upwind method. The under-relaxation factors are set as 0.3, 1, 1, 0.7, 0.9, and 1 for pressure, density, body forces, momentum, liquid fraction update, and energy, respectively. The convergence criteria for continuity, momentum, and energy equations are 10^{-4}, 10^{-4}, and 10^{-6}, respectively. The grid and time step independence tests are carried out to identify the suitable mesh size and time step. Three mesh sets (63,210 cells, 87,962 cells, and 128,591 cells) and time steps (0.5 s, 1 s, and 2 s) were tested. Figure 3 shows the variation of the liquid fraction (basalt; size: 20 mm; filling height: 112.0 mm) and indicates that the grid size and time step almost do not influence the liquid fraction. To balance the computational cost and accuracy, the medium mesh set (87,962 cells) and the time step of 1 s are used in the later simulation. The simulations are run on a workstation with 10 cores and 64 GB RAM, and each simulation takes 5 to 7 days. The parameters of the analysed configurations are summarised in Table 4.

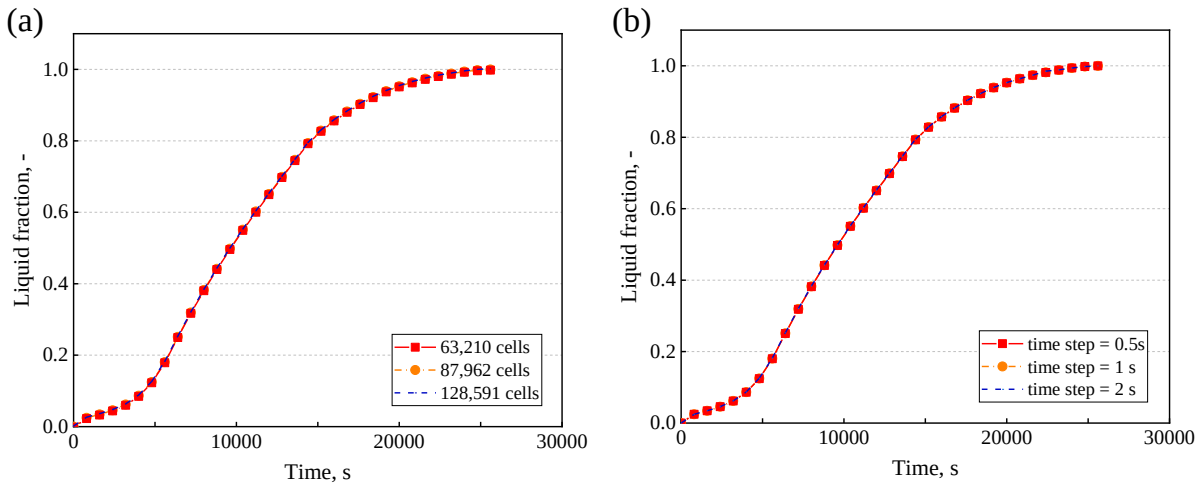

Figure 3. (a) Grid independence test; (b) time step independence test.

Table 4. Summary of the parameters of the analysed configurations.

Parameter	Inner diameter	Outer diameter	Number of the stone types	Filling height	Stone size
Value	40 mm	120 mm	6	0–112.0 mm	15–40 mm
Parameter	Porosity	Number of cases	Melting point of PCM	Initial temperature	Heating temperature
Value	0.5–1	15	54.4–64.1 °C	23 °C	75 °C

3. Model validation

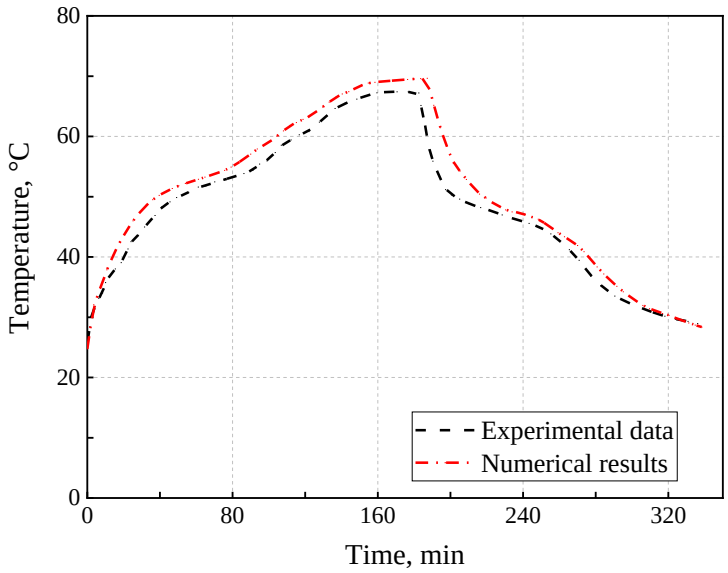

Figure 4. Validation of the Melting/Solidification model with Atal et al.'s experimental data [42].

The model validation consists of two parts, and the first one is the validation of the Melting/Solidification model. Atal et al. [42] conducted an experiment to study the phase change of paraffin in a shell-and-tube unit. The unit size, experimental conditions, and thermo-physical properties are listed in Tables 5 and 6. The authors first did the melting experiment, where the 70 °C air passed through the inner tube and heated the energy storage material with an initial temperature of 25 °C. When a steady state was reached, the hot air was replaced by the cold air (25 °C) to cool the energy storage material. The unit was wrapped in fibreglass to reduce heat loss to the environment. The authors placed K-type thermocouples at the midpoint between the inner and outer tubes and computed the average value of the recorded temperature. Figure 4 indicates that the numerical results are slightly higher than the experimental data. This is because there can be some heat loss in the experiment, while the boundary was set as adiabatic

in the numerical simulation. The average value of comparison results (10 min interval) between the numerical results and experimental data is 2.2 °C. The general trend of the numerical results agrees well with that of the experimental data, and the numerical results are almost the same as the experimental data at the last stage. Therefore, the Melting/Solidification model is verified.

Table 5. The unit size and experimental conditions in Ref. [42] and Ref. [43].

Parameter	Ref. [42]	Ref. [43]
Length of the tube, mm	762, 304.8 (inner, outer)	800, 500, 500 (inner, middle, outer)
Radius of the tube, mm	6.4, 25.4 (inner, outer)	25.4, 75, 100 (inner, middle, outer)
Thickness of the tube, mm	1.7, 1.3 (inner, outer)	1.2, 2, 2 (inner, middle, outer)
Initial temperature, °C	25	93
Heat transfer fluid	Air	Water
Temperature of HTF, °C	70, 25 (heating, cooling)	68

As most simulation cases are the stone/PCM configuration, the model of the stone/PCM configuration also needs to be validated. However, since the stone/PCM configuration is a novel structure, there is little experimental data in the open literature. The essence of the stone/PCM configuration is that the thermal enhancer increases the heating area of the PCM; as a result, the coupled boundary between the thermal enhancer and PCM is included in the numerical model. The heat storage unit with fins has the same principle, and the experimental results of this kind of unit were used to validate the stone/PCM configuration. As the Melting model has been validated in the last part, it is unnecessary to use the melting experiment again. Al-Abidi et al. [43] studied the solidification of paraffin in a shell-and-tube unit with internal and external fins. Tables 5 and 6 show the unit size, experimental conditions and thermo-physical properties. In Al-Abidi et al.'s research, a triplex concentric unit was fabricated where the energy storage material occupied the middle tube, and the HTF flowed through the inner and outer tubes. The average initial temperature of the energy storage material was 93 °C, and the 68°C water was pumped from a tank to the unit to cool the energy storage material. The temperature of the HTF

was maintained using an electrical heater and a thermostat controller in the water tank. The 15 thermocouples were placed in the PCM, and the average temperature was calculated. As shown in Figure 5, the numerical results agree well with the experimental data in the first 5 min; then, they are slightly higher, and the deviation gets larger with time. However, the deviation becomes smaller after 40 min, and the numerical result is almost the same as the experimental one at the end of the solidification. The average value of comparison results between the numerical results and experimental data is 1.8 °C, and the maximum deviation is less than 5%, demonstrating the feasibility of the current model.

Table 6. Thermo-physical properties in Ref. [42] and Ref. [43].

Property	Ref. [42]	Ref. [43]
Thermal conductivity of PCM, W/(m · K)	0.25	0.2
Specific heat of PCM, J/(kg · K)	2,510	2,000
Density of PCM, kg/m^3	730–790	950 (solid)/770 (liquid)
Melting temperature of PCM, °C	50–60	77–85
Latent heat of PCM, J/kg	117,000	176,000
Thermal conductivity of the fin, W/(m · K)	-	387.6
Specific heat of the fin, J/(kg · K)	-	381
Density of the fin, kg/m^3	-	8,978

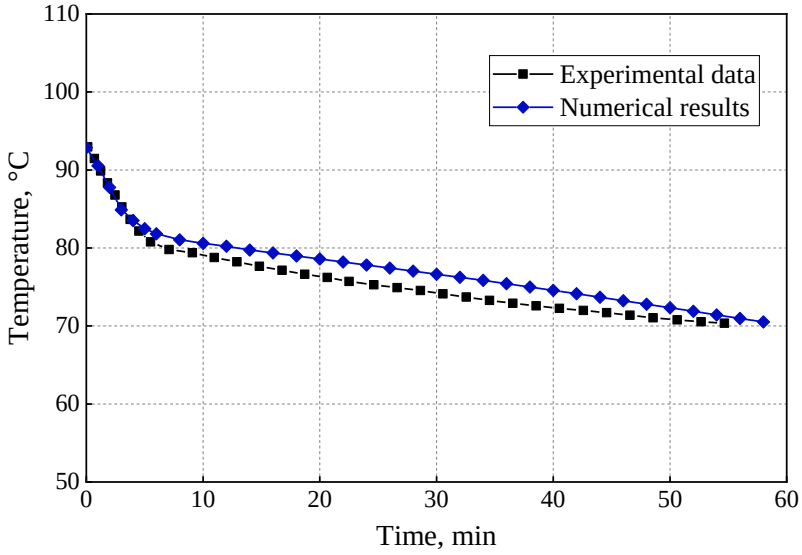

Figure 5. Model validation with Al-Abidi et al.'s experimental data [43].

4. Results and discussions

4.1 Effect of stone types

The melting front of the PCM is shown in Figure 6. The selected plane for result visualisation is at half the thickness, and the schematic of the slice location is presented in Figure S2. At the initial stage (5000 s), the contact melting mode between the PCM and the tube dominates heat transfer; therefore, the PCM around the tube is melted first. Taking basalt as an example, the temperature of the PCM around the tube is higher than $T_{m,l}$; thus, φ of cells is 1, as indicated by Eq. (5), and this part of the PCM shows the liquid state. The temperature of the PCM in the gap between stones is between $T_{m,l}$ and $T_{m,s}$; therefore, φ of cells is higher than 0 and lower than 1 according to Eq. (5), and this part of the PCM shows the mushy state. The temperature of the PCM near the shell is lower than $T_{m,s}$, and this part of the PCM cannot melt under such low temperature; thus, φ of cells is 0, and the PCM shows the solid state. With the elapse of time (10000 s), the PCM in the upper region is melted rapidly, and all the PCM is liquid or mushy. The thermal conductivity of stones is high, and the contact area between stones and the PCM is large, which helps transfer the HTF's heat; as a result, the PCM around stones has a higher melting rate. All the PCM in the upper half is melted at 20000 s, and the part in the

lower half is highly mushy. The PCM at the bottom of the heat storage unit is rarely influenced by natural convection, and as the thermal conductivity is low, it usually melts very slowly. However, in the stone/PCM configuration, the bottom stones are in contact with the tube and transfer the HTF's heat to the PCM; thus, the bottom PCM melts fast and is highly mushy at 20000 s.

The difference in the melting front between the four cases becomes significant at 15000 s; the melting front of the PCM with basalt develops the slowest, while that with granite develops the fastest. Actually, the thermal conductivity of basalt (3.2 W/(m · K)) is higher than that of granite (2.86 W/(m · K)). The specific heat of basalt is higher, and much of the absorbed heat is stored in stones rather than transferred to the PCM, leading to the slow development of the melting front.

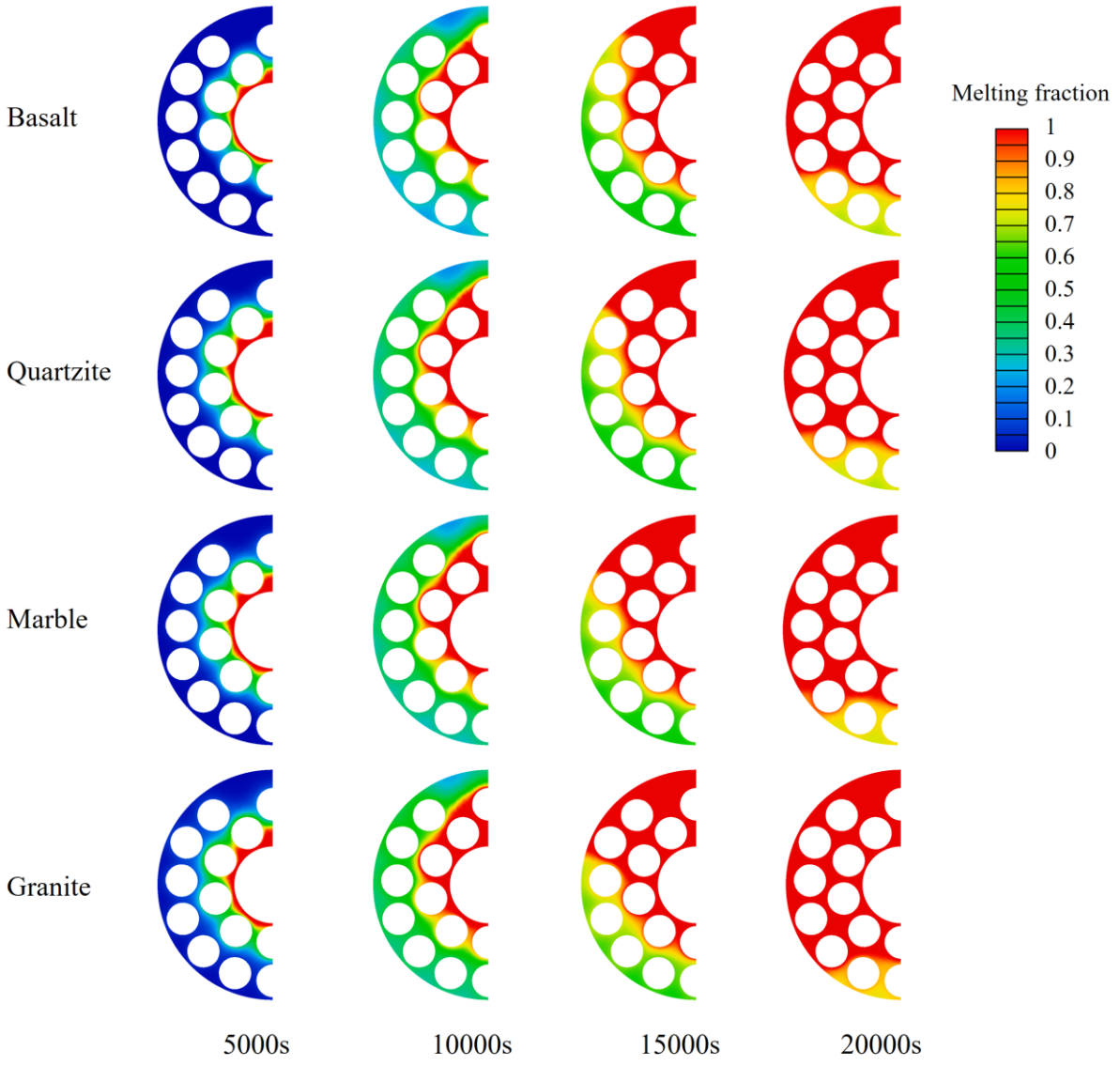

Figure 6. Melting front of the PCM with different types of stones (the plane of half the thickness).

As shown in Figure 7, the PCM around the tube generally has the highest velocity during the whole melting process. Taking quartzite as an example, the PCM around the tube is liquid at 10000 s, and its velocity is high. The PCM in the gap between stones is mushy, and its velocity is lower, which is governed by terms $\frac{(1-\varphi)^2}{(\varphi^3+\omega)}A_{\text{mushy}}u$ and $\frac{(1-\varphi)^2}{(\varphi^3+\omega)}A_{\text{mushy}}v$ in Eqs. (2)-(3). That is because the flow resistance in the mushy zone is high, leading to a lower velocity. At 15000 s, the overall velocity field of the PCM is improved, and the natural convection is enhanced; the velocity in the gap is high, which is beneficial to natural convection and helps transfer stones' heat to the PCM. However, the velocity around the tube is decreased at 20000

s because the difference in the density of the liquid PCM gets insignificant after a long time of heat and mass transfer.

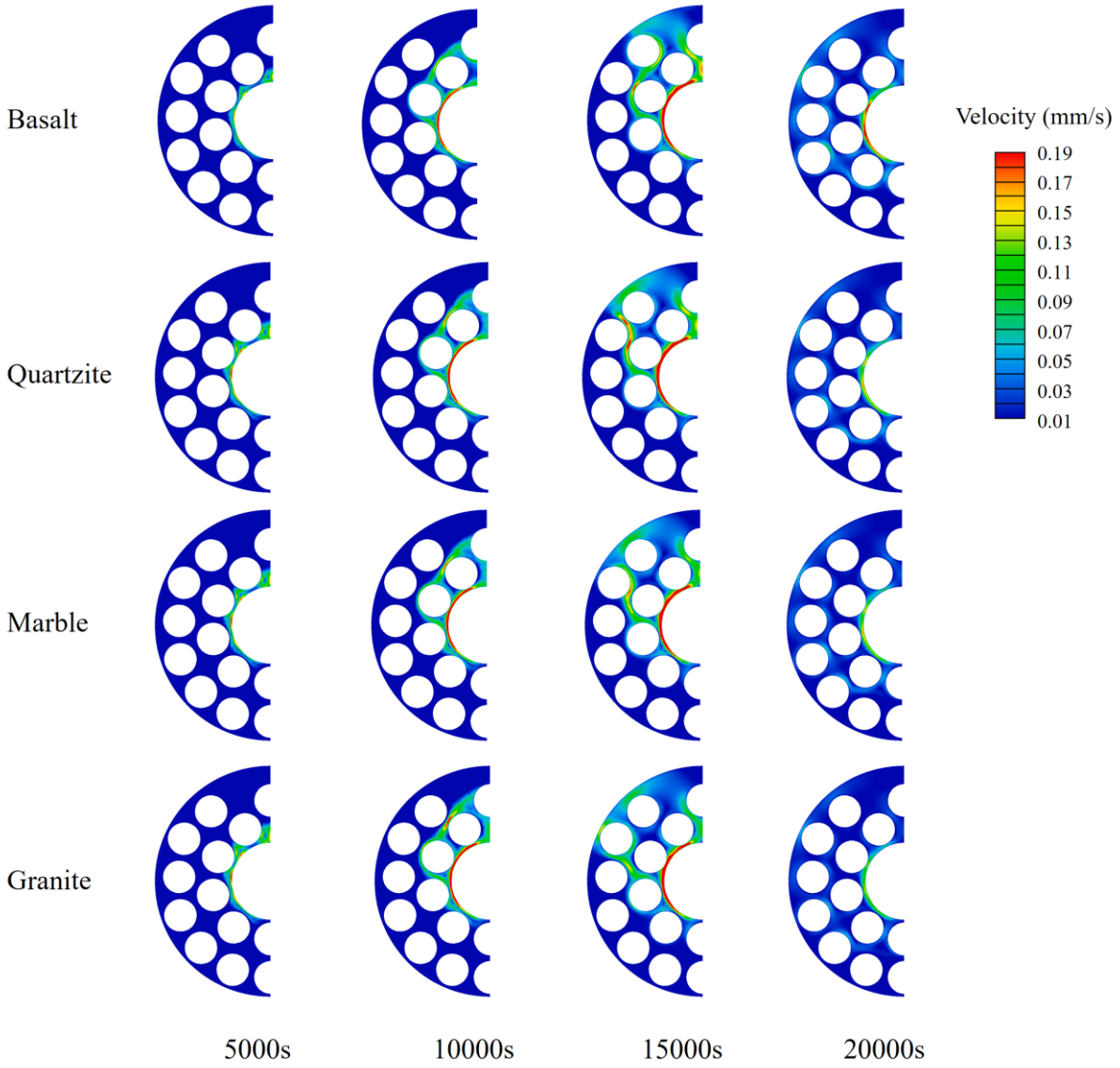

Figure 7. Velocity distribution of the PCM with different types of stones.

The temperature field is shown in Figure 8, where the PCM around the tube has the highest temperature. With the elapse of time (10000 s), the temperature increases and is higher than the liquidus temperature ($T_{m,\,l}$, 64.1 °C). As a result, the buoyancy force starts to work, which is governed by the term $\rho_{PCM}\, g\, \beta(T - T_{m1})$ in Eq. (3). The density of the hot PCM is low, so it flows upwards under the buoyancy force. The temperature at the top region increases remarkably at 15000 s, which is attributed to natural convection. As the melting further

proceeds, the whole temperature field is improved, and the temperature of the PCM in the upper half is significantly higher than that in the lower half. The temperature field in the lower half is uniform, probably because stones enhance the heat transfer at the bottom of the heat storage unit and improve the temperature of the bottom PCM. Like the melting front, the difference in the temperature field between the four cases becomes significant at 15000 s.

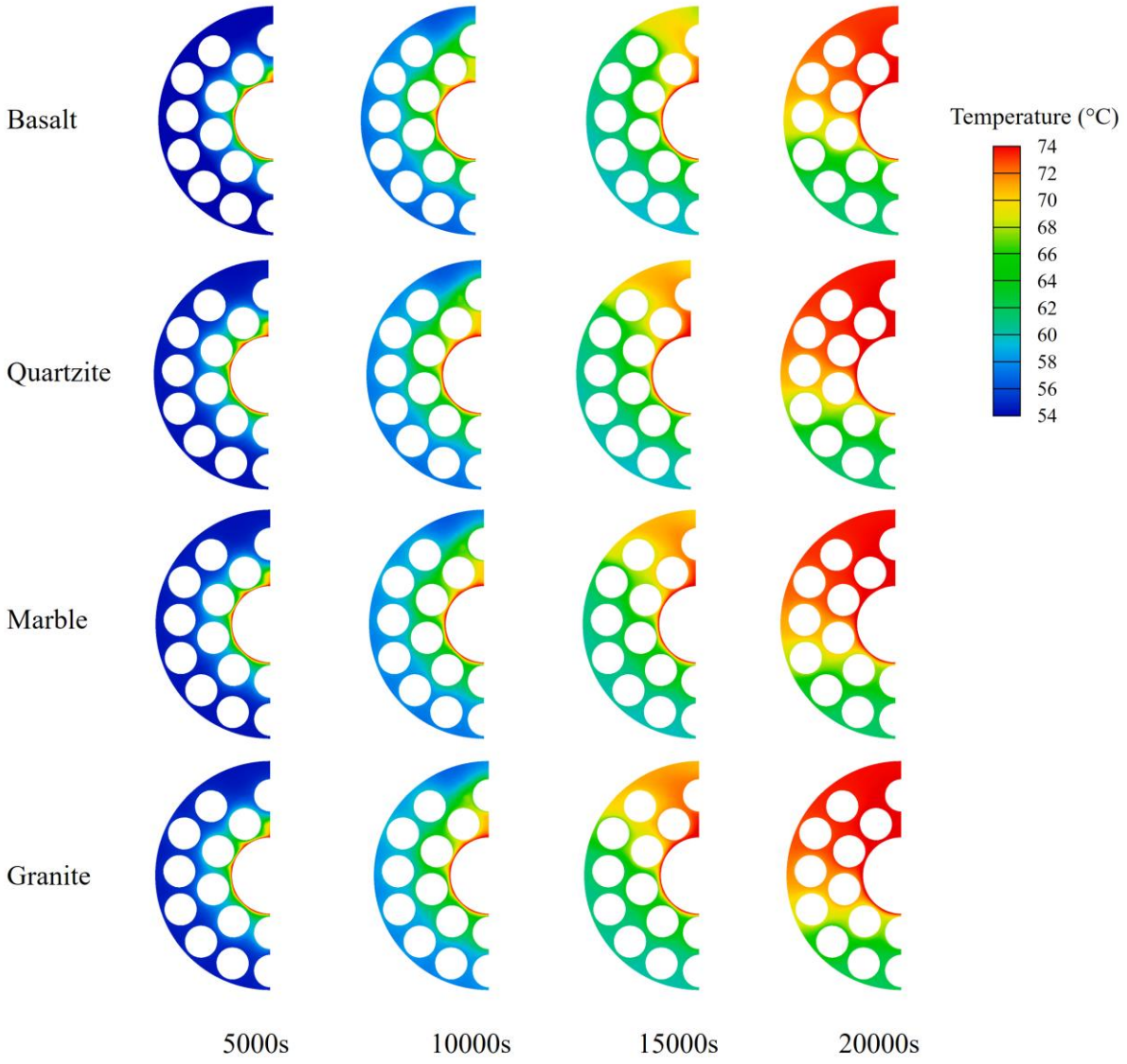

Figure 8. Temperature distribution of the PCM with different types of stones.

The melting rate, stored energy, and exergy are calculated based on a complete unit with a length of 40 mm. The melting rate (v) is calculated by:

$$v = \frac{V_{\mathrm{PCM}}}{t_{\mathrm{m}}} \tag{13}$$

The increase in the melting rate (x_i) is calculated by:

$$x_i = \frac{v_i - v_0}{v_0} \times 100\% \quad (14)$$

where V_{PCM} is the volume of PCM; t_m is the total melting time; v_0 is the melting rate of the unit without stones; v_i is the melting rate of the unit with stones (i represents granite, gneiss, marble, sandstone, quartzite, or basalt). Figure 9(a) indicates that all cases with stones have a higher melting rate than that without stones, and x_i is at least 86.7%. The order of x_i from high to low is granite, gneiss, marble, sandstone, quartzite, and basalt. However, the order of thermal conductivity is different: basalt, granite, gneiss, marble, quartzite, and sandstone. It can be explained as follows: the melting rate is more related to heat rather than energy; thermal diffusivity measures the heat transfer rate, and the order of thermal diffusivity from high to low is: granite (1.32×10^{-6} m^2/s), gneiss (1.23×10^{-6} m^2/s), marble (1.21×10^{-6} m^2/s), sandstone (1.17×10^{-6} m^2/s), quartzite (1.00×10^{-6} m^2/s), basalt (0.82×10^{-6} m^2/s), which is consistent with the order of x_i.

Nevertheless, the PCM/basalt configuration can store thermal energy faster, and its advantage is very significant (Figure 9(b)). As seen in Figure 9(c), the energy stored by PCM in the six cases is almost identical, while the energy stored by stones is distinct. The energy stored by basalt is more than two times that of sandstone because basalt has a higher specific heat. The basalt/PCM configuration has the maximum total stored energy, 32.3% higher than the sandstone/PCM configuration. The effect of the stone type on the energy storage rate is shown in Figure S3. Basalt causes the highest energy storage rate, followed by gneiss, granite, marble, quartzite, and sandstone. The increase in the energy storage rate is more significant than that in the melting rate; taking basalt as an example, the increase in the energy storage rate is 215.8%, while that in the melting rate is only 86.7%. That is because the sensible heat energy stored by stones is included in the energy storage rate, which increases the total stored energy.

The exergy is calculated by [17]:

$$Ex = \int_0^t \left[\left(1 - \frac{T_0}{T_{\mathrm{PCM}}}\right) m_{\mathrm{PCM}} c_{\mathrm{p,\ PCM}} \frac{dT_{\mathrm{PCM}}}{dt} + \left(1 - \frac{T_0}{T_{\mathrm{m}}}\right) \rho_{\mathrm{PCM}} L \frac{df_{\mathrm{l}}}{dt} + \left(1 - \frac{T_0}{T_{\mathrm{stone}}}\right) m_{\mathrm{stone}} c_{\mathrm{p,\ stone}} \frac{dT_{\mathrm{stone}}}{dt} \right] dt \quad (15)$$

where T_0 is the reference temperature assumed to be 23 °C in the current study. T_{m} is the average melting temperature of the PCM; f_{l} is the overall liquid fraction.

The exergy variation with time is plotted in Figure 9(d). Although the difference in energy curves of the six configurations is significant, the exergy curves differ insignificantly (Figure 9(d)), and the total exergy is nearly identical (Figure 9(e)). Compared to the only PCM configuration, the exergy storage rate of all the PCM/stone configurations is increased by more than 200% (Figure S4). And the granite/stone configuration has the highest exergy storage rate, 246.4% higher than the only PCM configuration. Granite has the highest thermal diffusivity (1.32×10^{-6} m^2/s), which relates to the heat transfer rate directly; as a result, the complete melting time of the PCM is the shortest, and the melting rate is the highest.

For the economic analysis, the price of paraffin and stones varies according to location, season, market, etc., which makes it hard to get a specific and accurate figure for the price. However, the price of materials within one country is relatively stable; hence, the price of materials in the same country is selected (Table 6). The following economic analysis aims to provide a general overview of economics.

Table 7. Price of heat storage materials.

Type	Paraffin [44]	Basalt [45]	Granite [46]	Gneiss [47]	Marble [48]	Quartzite [49]	Sandstone [50]
Price (£/ton)	985.7	22.0	6.3	12.6	58.5	22.0	7.1

An energy storage economic index, which characterises the amount of effective thermal energy stored per unit of time and unit cost, is defined as:

$$\vartheta = \frac{Ex}{(p_{\mathrm{PCM}} + p_{\mathrm{stone}})\, t_{\mathrm{m}}} \quad (16)$$

where Ex is the total exergy; p_{PCM} and p_{stone} are the cost of the PCM and stones, respectively. The total exergy rather than the total energy is taken as the numerator because exergy directly measures the amount of energy which can be extracted for application. Figure 9(f) indicates that all the PCM/stone configurations are more cost-effective than the pure PCM. That is because the exergy storage rate is increased, and the cost of storage materials is decreased. ϑ is increased by at least 439%. The PCM/granite configuration is the most cost-effective, with a 552% increase in ϑ.

As the density of stones is higher than that of paraffin, the PCM/stone configuration would increase the mass. Figure S5 shows the mass of different configurations and indicates that the mass of the PCM/stone configuration almost doubles that of the case without stones. The PCM/gneiss configuration is the heaviest, the mass of which is increased by 117%. The application scenario of the PCM/stone configuration is the immobilized TES, such as thermal energy storage for residential buildings [51] and in-place waste heat recovery [29], removing the worry about the portability problem.

Various heat transfer enhancement methods (using metal foam, ceramic foam, fins, nanoparticles, heat pipes, and natural stones) are compared, and the performance and cost are shown in Table S2–S5. Natural stones are not as good as metal foam in energy storage rate but are better than ceramic foam, fins, nanoparticles, and heat pipes. Conventional methods increase the material cost, with a maximum increase of over 276 times (copper foam). In comparison, the PCM/stone configuration decreases the material cost because natural stones are much cheaper than the PCM. The performance and cost make the PCM/stone configuration a competitive candidate for thermal energy storage.

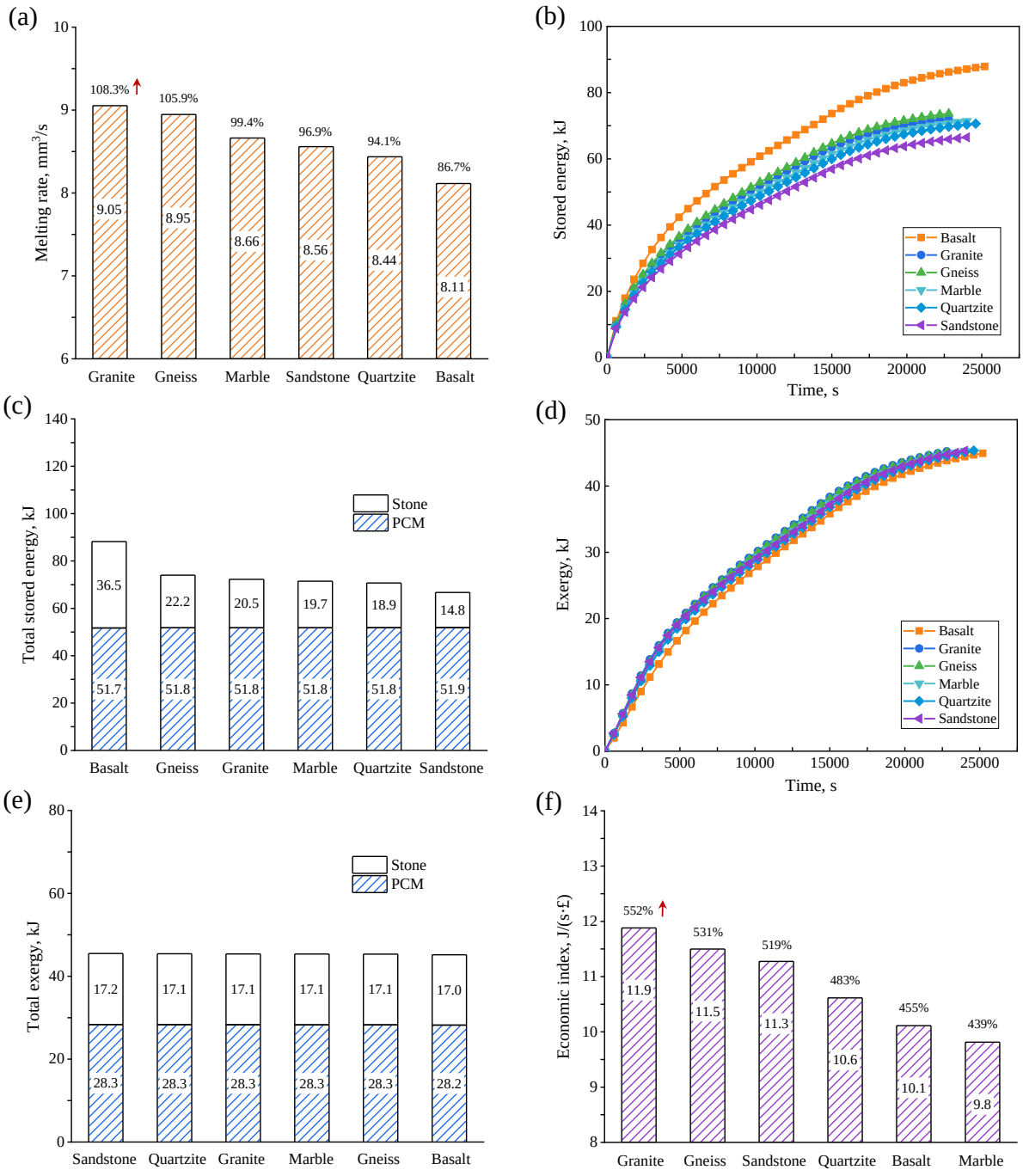

Figure 9. (a) Effect of the stone type on the melting rate and the increase compared to the case without stones; (b) stored energy variation with time; (c) effect of the stone type on the total stored energy; (d) exergy variation with time; (e) influence of the stone type on the total exergy; (f) effect of the stone type on the energy storage economic index and the increase compared to the case without stones.

4.2 Effect of filling height

Figure S6 shows the melting front under different filling heights (granite). At 5000 s, the PCM around the tube is melted first; some PCM around stones is mushy, and the amount of the mushy PCM increases as the filling height. At 10000 s, more PCM around the tube is melted, and most of the PCM around the stones is mushy. Stones help transfer the tube's heat to the PCM, and the temperature of the bottom PCM rises rapidly; as a result, this part of the PCM melts fast. Figure S7 suggests that the velocity of the mushy PCM is low, indicating heat conduction is the primary heat transfer mechanism. As the filling height increases, the amount of the solid PCM decreases. For the filling height of 46.0 mm and 62.9 mm, the difference in the flow field at 10000 s is insignificant. That is because stones are in the lower half and have little effect on the flow field. The dominant heat transfer modes differ between the only-PCM region and the stone-filling region: the velocity of the liquid PCM is high in the former, indicating natural convection is strong. The velocity is low in the latter; however, stones with high thermal conductivity enhance heat conduction, so the temperature also rises rapidly. As the filling height increases, the heat conduction is enhanced more significantly, and the temperature rises faster. For the filling height of 46.0 mm, there is much solid PCM at 15000 s, while for that of 97.0 mm, the solid PCM disappears. The velocity of the PCM in the former case is low (Figure S6), which may be caused by the limited flow space; by contrast, the velocity in the latter case is higher, and the temperature distribution is more uniform (Figure S7).

At 20000 s, most PCM in the case of 97.0 mm is melted, while there is still some solid PCM in the case of 46.0 mm. For the former case, the velocity of the PCM in the upper half is decreased because the temperature difference is insignificant after a long-time heat exchange. For the latter case, the velocity is increased because the flow space is extended.

The melting volume variation with time is plotted in Figure 10(a). In the initial stage, there is no significant difference between the five cases because the PCM around the tube is melted

first, as indicated in Figure S6. After 5000 s, the difference in the melting volume becomes significant, and the higher the filling height, the faster the melting volume increases. It is noted that the difference between cases of 97.0 mm and 112.0 mm is insignificant because natural convection in the top region is strong, and the heat transfer enhancement by stones balances the loss in natural convection. The same phenomenon can be found in the exergy variation (Figure 10 (c)).

Different filling heights mean different amounts of PCM; hence, the stored energy is different. As shown in Figure 10(b), the energy stored by the PCM decreases with the filling height, while that by stones increases. And the total stored energy decreases significantly with the filling height, while the total exergy is affected insignificantly (Figure 10(d)). That may be because the energy stored by stones is high-quality, about 80% of which is exergy; by contrast, only about 50% of the energy stored by the PCM is exergy.

Figure 10(e) indicates that the exergy storage rate of cases with stones is increased, and the higher the filling height, the higher the exergy storage rate. The exergy storage rate for the case of 112.0 mm is the highest, which is increased by 246% compared to the one without stones. Moreover, since the cost of stones is low, the economics is further improved. As seen in Figure 10(f), $\mathcal{I}$ in the case of 112.0 mm is increased by 552%.

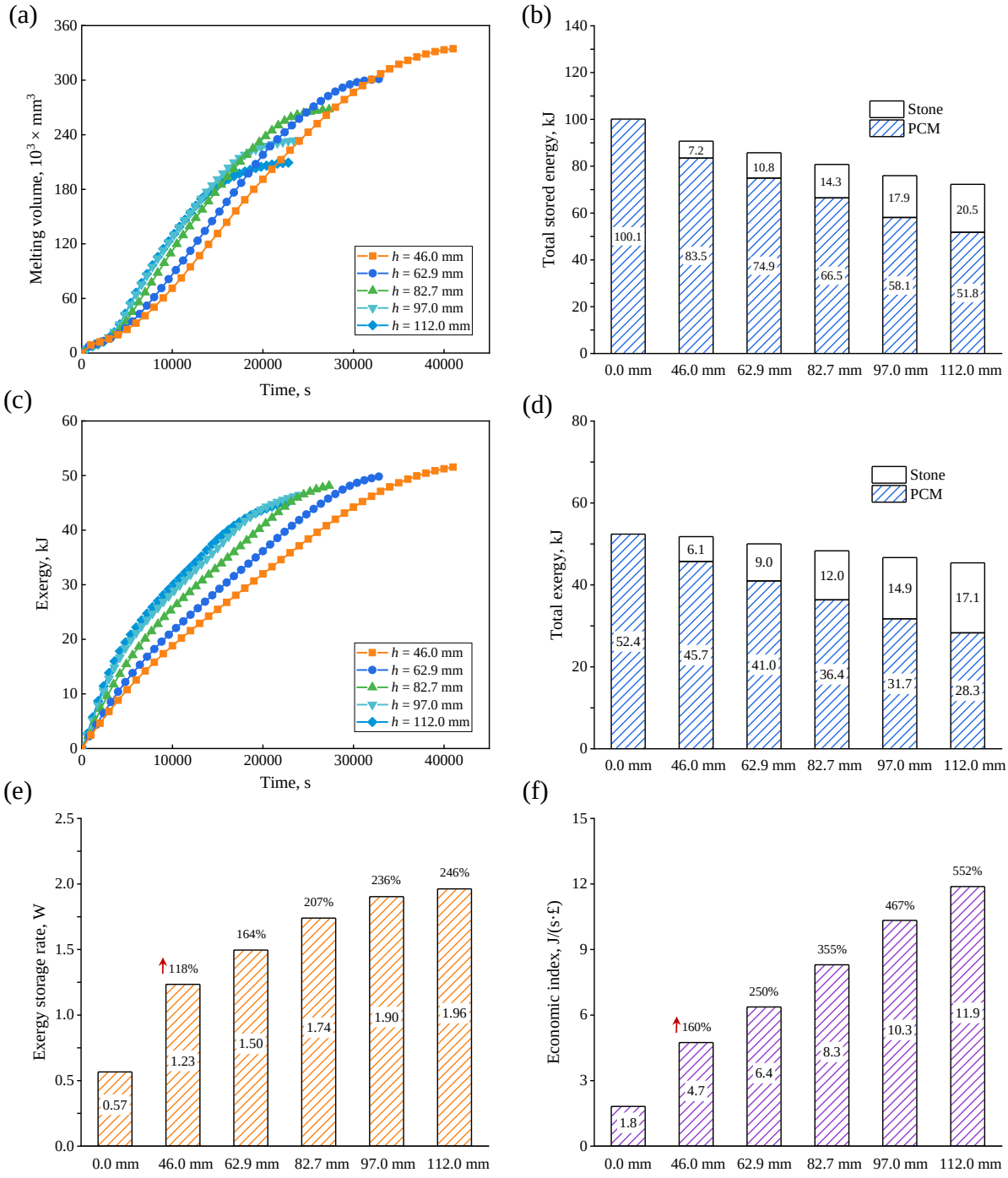

Figure 10. (a) The melting volume variation with time; (b) effect of the filling height on the total stored energy; (c) exergy variation with time; influence of the filling height on (b) total exergy, (e) exergy storage rate, and (f) energy storage economic index.

4.3 Effect of stone sizes

It is seen from Figure S9 that the PCM with 15 mm-sized stones is melted fast, and all PCM is liquid or mushy at 10000 s. At 20000 s, the difference in the melting front is significant:

for the cases of 15 mm and 40 mm, most PCM has been melted completely, while for those of 25 mm and 30 mm, about half of PCM is mushy.

Figure S10 shows the velocity distribution of the PCM. As more PCM is melted at 10000 s, the flow space in all cases is extended, and the velocity is increased. At 15000 s, the flow space is further extended, and the velocity field in the cases of 25 mm and 30 mm is improved. However, as the melting proceeds (20000 s), the velocity in the case of 40 mm is decreased significantly because all PCM in the upper half is almost melted at 15000 s, and the temperature difference becomes small after a long-time heat exchange.

Figure S11 suggests that at 5000 s, the difference in the temperature field between the four cases is insignificant, whereas, at 10000 s, the difference is remarkable, especially for the PCM near the shell. As the melting proceeds (15000 s), the temperature of PCM increases. For the cases of 25 mm and 30 mm, the temperature in the upper half increases remarkably, while that in the lower half increases insignificantly because stones in the lower half are not in contact with the inner tube and cannot conduct its heat. The variation of the temperature field at 20000 s is similar, and the reason is identical.

The 15 mm-sized stones accelerate the melting of PCM most significantly, but the total stored energy is slightly lower than the case of 30 mm (Figure 11(a)-(b)). The porosity in the case of 20 mm (0.52) is slightly lower than that in the case of 15 mm (0.55), suggesting there are more stones in the former case, and the heat transfer rate should have been higher than in the latter case. However, Figure 11(a) shows the opposite results. It is probably because the smaller stones have larger surface areas, which is beneficial for heat transfer. As shown in Figure 11(c), the exergy in cases of 15 mm, 20 mm, and 40 mm varies similarly and is higher than that in cases of 25 mm and 30 mm. Taking cases of 20 mm and 25 mm as examples, the porosity in the former case is 0.52 while that in the latter case is 0.61; namely, there are more stones in the case of 20 mm, which leads to higher heat transfer enhancement performance.

Additionally, more stones surround the tube in the case of 20 mm and transfer the tube's heat; as a result, their temperature is higher (Figure 11(d)), contributing to faster exergy storage.

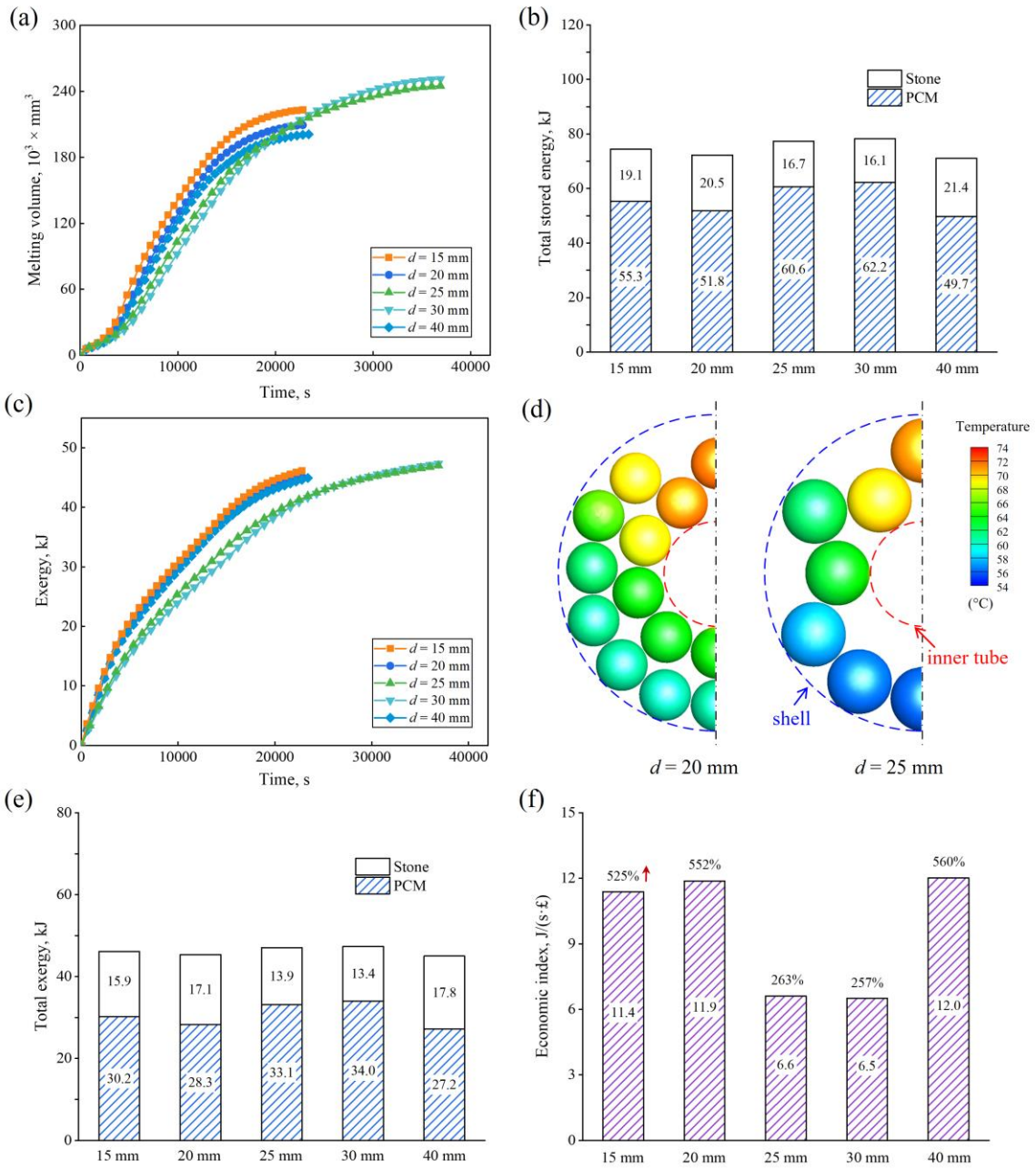

Figure 11. (a) The melting volume variation under different stone sizes; (b) effect of the stone size on the total stored energy; (c) the exergy variation with time; (d) temperature distribution of stones at 15000 s; (e) influence of the stone size on the total exergy; (f) influence of the stone size on the energy storage economic index and the increase compared to the case without stones.

It is seen from Figure 11(e) that the total exergy in the case of 40 mm is 45.0 kJ (the minimum), which is only 5.1% lower than that in the case of 30 mm (47.4 kJ, the maximum), suggesting the total exergy is hardly influenced by the stone size. By contrast, the economic index is affected significantly. As shown in Figure 11(f), the energy storage economic indices for cases of 15 mm, 20 mm, and 40 mm are much higher than the other two cases. The economic index for the case of 40 mm is the highest, increasing by 560% compared to the one without stones. 40 mm equals the equivalent radius of the annular space (inner radius: 20 mm; outer radius: 60 mm); stones fit with the annular space and are in good contact with the inner tube, which transfers the tube's heat efficiently and increases the exergy storage rate significantly. Moreover, using stones decreases the material cost, further improving the economy. It is noted that the economic index of all cases with stones is increased, and the minimum is 257%.

5. Conclusions

Natural stones acted as sensible heat storage media for packed beds in previous studies. In this study, they are used to enhance the heat transfer of the PCM in latent heat storage. Natural stones and PCM fill the annular space of a shell-and-tube unit, forming a hybrid sensible-latent heat storage configuration. Stones not only act as sensible heat storage media (the original role) but also as thermal enhancers (the new role). Different stone types, filling heights, and sizes are tested based on a 3D numerical simulation, and a comprehensive energy, exergy, and economic analysis is performed. The following conclusions are drawn:

(1) Basalt, quartzite, sandstone, marble, gneiss, and granite save the charging time by 72.1%, 73.2%, 73.6%, 73.9%, 74.7%, and 75.0%, respectively, compared to the case without stones. Granite has the best heat transfer enhancement performance owing to superior thermal diffusivity and increases the melting rate by 108%. Basalt with high specific heat contributes to the large energy capacity, improving the melting rate by 87% in comparison with the case without stones.

(2) The energy stored by the PCM decreases with the filling height, while that by stones increases. The total energy decreases significantly with the filling height, whereas the exergy varies insignificantly. The exergy storage rate with a filling height of 112.0 mm is increased by 246%.

(3) The total exergy is hardly influenced by the stone size, and the minimum is only 5.1% lower than the maximum. Stones surrounding the inner tube are beneficial to the exergy storage rate. The energy storage economic index is improved by at least 257%; the 40 mm-sized stones (equal to the equivalent radius of the annular space) are the most cost-effective, and a 560% increase in the economy is achieved.

Natural stones are proven to enhance the heat transfer of the PCM significantly. Moreover, they are widely accessible, low-cost, and environmentally friendly, which makes them promising in latent heat thermal energy storage applications.

Acknowledgements

The work was supported by H2020-MSCA-RISE-778104–ThermaSMART, doctoral degree scholarship of China Scholarship Council (CSC).

Nomenclature

HTF	Heat transfer fluid
LHTES	Latent heat thermal energy storage
PCM	Phase change material
SHM	Sensible heat storage material
SHTES	Sensible heat thermal energy storage
TES	Thermal energy storage
TRTES	Thermochemical reaction thermal energy storage
A_{mushy}	Mushy zone constant
c_{p}	Specific heat capacity
Ex	Exergy
f_{l}	Overall liquid fraction
g	Gravitational acceleration
L	Latent heat
T	Temperature
T_0	Reference temperature
T_{m}	Average melting temperature of phase change material
$T_{\text{m, l}}$, $T_{\text{m, u}}$	Lower limit and upper limit of the melting point
u, v, w	Velocity in x, y and z direction

Greek letter

ω	A small number
β	Thermal expansion coefficient
μ	Viscosity

ρ	Density
k	Thermal conductivity
φ	Liquid fraction in the cell

References

[1] S. Zhang, Z. Li, Y. Yao, L. Tian, Y. Yan, Heat transfer characteristics and compatibility of molten salt/ceramic porous composite phase change material, Nano Energy, 100 (2022) 107476.

[2] A.M. Abdulateef, S. Mat, J. Abdulateef, K. Sopian, A.A. Al-Abidi, Geometric and design parameters of fins employed for enhancing thermal energy storage systems: a review, Renewable and Sustainable Energy Reviews, 82 (2018) 1620-1635.

[3] S. Zhang, D. Feng, L. Shi, L. Wang, Y. Jin, L. Tian, Z. Li, G. Wang, L. Zhao, Y. Yan, A review of phase change heat transfer in shape-stabilized phase change materials (ss-PCMs) based on porous supports for thermal energy storage, Renewable and Sustainable Energy Reviews, 135 (2021) 110127.

[4] S.F. Ahmed, M. Khalid, W. Rashmi, A. Chan, K. Shahbaz, Recent progress in solar thermal energy storage using nanomaterials, Renewable and Sustainable Energy Reviews, 67 (2017) 450-460.

[5] S. Kuravi, J. Trahan, D.Y. Goswami, M.M. Rahman, E.K. Stefanakos, Thermal energy storage technologies and systems for concentrating solar power plants, Progress in Energy and Combustion Science, 39 (2013) 285-319.

[6] W. Wang, X. He, Y. Shuai, J. Qiu, Y. Hou, Q. Pan, Experimental study on thermal performance of a novel medium-high temperature packed-bed latent heat storage system containing binary nitrate, Applied Energy, 309 (2022) 118433.

[7] H. Zhang, J. Baeyens, G. Cáceres, J. Degreve, Y. Lv, Thermal energy storage: Recent developments and practical aspects, Progress in Energy and Combustion Science, 53 (2016) 1-40.

[8] P.L. Singh, S.D. Deshpandey, P.C. Jena, Thermal performance of packed bed heat storage system for solar air heaters, Energy for Sustainable Development, 29 (2015) 112-117.

[9] R. Lugolole, A. Mawire, D. Okello, K.A. Lentswe, K. Nyeinga, A.B. Shobo, Experimental analyses of sensible heat thermal energy storage systems during discharging, Sustainable Energy Technologies and Assessments, 35 (2019) 117-130.

[10] M.S. Audi, Experimental study of a solar space heating model using Jordanian rocks for storage, Energy Conversion and Management, 33 (1992) 833-842.

[11] R. Tiskatine, R. Oaddi, R. Ait El Cadi, A. Bazgaou, L. Bouirden, A. Aharoune, A. Ihlal, Suitability and characteristics of rocks for sensible heat storage in CSP plants, Solar Energy Materials and Solar Cells, 169 (2017) 245-257.

[12] S. Soprani, F. Marongiu, L. Christensen, O. Alm, K.D. Petersen, T. Ulrich, K. Engelbrecht, Design and testing of a horizontal rock bed for high temperature thermal energy storage, Applied Energy, 251 (2019) 113345.

[13] G. Alva, Y. Lin, G. Fang, An overview of thermal energy storage systems, Energy, 144 (2018) 341-378.

[14] S. Zhang, Z. Li, H. Wang, L. Tian, Y. Jin, M. Alston, Y. Yan, Component-dependent thermal properties of molten salt eutectics for solar thermal energy storage: experiments, molecular simulation and applications, Applied Thermal Engineering, (2022) 118333.

[15] N.I. Ibrahim, F.A. Al-Sulaiman, S. Rahman, B.S. Yilbas, A.Z. Sahin, Heat transfer enhancement of phase change materials for thermal energy storage applications: A critical review, Renewable and Sustainable Energy Reviews, 74 (2017) 26-50.

[16] Y. Yao, H. Wu, Interfacial heat transfer in metal foam porous media (MFPM) under steady thermal conduction condition and extension of Lemlich foam conductivity theory, International Journal of Heat and Mass Transfer, 169 (2021) 120974.

[17] S. Zhang, Y. Yan, Energy, exergy and economic analysis of ceramic foam-enhanced molten salt as phase change material for medium- and high-temperature thermal energy storage, Energy, 262 (2023) 125462.

[18] Z. Liu, Y. Yao, H. Wu, Numerical modeling for solid–liquid phase change phenomena in porous media: Shell-and-tube type latent heat thermal energy storage, Applied Energy, 112 (2013) 1222-1232.

[19] S. Zhang, Y. Yan, Evaluation of discharging performance of molten salt/ceramic foam composite phase change material in a shell-and-tube latent heat thermal energy storage unit, Renewable Energy, 198 (2022) 1210-1223.

[20] X. Yang, Z. Lu, Q. Bai, Q. Zhang, L. Jin, J. Yan, Thermal performance of a shell-and-tube latent heat thermal energy storage unit: Role of annular fins, Applied Energy, 202 (2017) 558-570.

[21] Y. Huang, X. Liu, Charging and discharging enhancement of a vertical latent heat storage unit by fractal tree-shaped fins, Renewable Energy, 174 (2021) 199-217.

[22] J.M. Mahdi, H.I. Mohammed, E.T. Hashim, P. Talebizadehsardari, E.C. Nsofor, Solidification enhancement with multiple PCMs, cascaded metal foam and nanoparticles in the shell-and-tube energy storage system, Applied Energy, 257 (2020) 113993.

[23] M. Parsazadeh, X. Duan, Numerical study on the effects of fins and nanoparticles in a shell and tube phase change thermal energy storage unit, Applied Energy, 216 (2018) 142-156.

[24] H. Shabgard, T.L. Bergman, N. Sharifi, A. Faghri, High temperature latent heat thermal energy storage using heat pipes, International Journal of Heat and Mass Transfer, 53 (2010) 2979-2988.

[25] K. Nithyanandam, R. Pitchumani, Computational studies on a latent thermal energy storage system with integral heat pipes for concentrating solar power, Applied Energy, 103 (2013) 400-415.

[26] Z. Duan, Z. Zhang, J. Wang, X. Cao, J. Zhang, Thermal performance of structured packed bed with encapsulated phase change materials, International Journal of Heat and Mass Transfer, 158 (2020) 120066.

[27] W.-J. Luo, P. Vishwakarma, B. Panigrahi, Hydrodynamic influence on thermal management of flexible heatsink devices embedded with out-of-plane intricate microchannel design, International Communications in Heat and Mass Transfer, 144 (2023) 106792.

[28] P. Zhang, Z.N. Meng, H. Zhu, Y.L. Wang, S.P. Peng, Melting heat transfer characteristics of a composite phase change material fabricated by paraffin and metal foam, Applied Energy, 185 (2017) 1971-1983.

[29] Y. Huang, Z. Deng, Y. Chen, C. Zhang, Performance investigation of a biomimetic latent heat thermal energy storage device for waste heat recovery in data centers, Applied Energy, 335 (2023) 120745.

[30] A. Gautam, R.P. Saini, A review on sensible heat based packed bed solar thermal energy storage system for low temperature applications, Solar Energy, 207 (2020) 937-956.

[31] Y. Jemmal, N. Zari, M. Maaroufi, Thermophysical and chemical analysis of gneiss rock as low cost candidate material for thermal energy storage in concentrated solar power plants, Solar Energy Materials and Solar Cells, 157 (2016) 377-382.

[32] J. Yang, L. Yang, C. Xu, X. Du, Numerical analysis on thermal behavior of solid–liquid phase change within copper foam with varying porosity, International Journal of Heat and Mass Transfer, 84 (2015) 1008-1018.

[33] R. Ge, Q. Li, C. Li, Q. Liu, Evaluation of different melting performance enhancement structures in a shell-and-tube latent heat thermal energy storage system, Renewable Energy, 187 (2022) 829-843.

[34] L. Pu, S. Zhang, L. Xu, Z. Ma, X. Wang, Numerical study on the performance of shell-and-tube thermal energy storage using multiple PCMs and gradient copper foam, Renewable Energy, 174 (2021) 573-589.

[35] Y. Yao, H. Wu, Macroscale Modeling of Solid–Liquid Phase Change in Metal Foam/Paraffin Composite: Effects of Paraffin Density Treatment, Thermal Dispersion, and Interstitial Heat Transfer, Journal of Thermal Science and Engineering Applications, 13 (2021).

[36] J.M. Mahdi, E.C. Nsofor, Solidification enhancement in a triplex-tube latent heat energy storage system using nanoparticles-metal foam combination, Energy, 126 (2017) 501-512.

[37] Ansys Help: The Boussinesq Model, https://ansyshelp.ansys.com/account/secured?returnurl=/Views/Secured/corp/v211/en/flu_ug/flu_ug_sec_hxfer_buoy.html?q=Boussinesq, 2023.

[38] S. Zhang, Z. Li, Y. Yan, M. Alston, L. Tian, Comparative study on heat transfer enhancement of metal foam and fins in a shell-and-tube latent heat thermal energy storage unit, Energy Storage and Saving, 2 (2023) 487-494.

[39] ANSYS FLUENT Theory Guide, https://www.afs.enea.it/project/neptunius/docs/fluent/html/th/node352.htm, 2023.

[40] M. Caliano, N. Bianco, G. Graditi, L. Mongibello, Analysis of a phase change material-based unit and of an aluminum foam/phase change material composite-based unit for cold thermal energy storage by numerical simulation, Applied Energy, 256 (2019) 113921.

[41] S. Zhang, Y. Yan, Thermal performance of latent heat energy storage system with/without enhancement under solar fluctuation for Organic Rankine power cycle, Energy Conversion and Management, 270 (2022) 116276.

[42] A. Atal, Y. Wang, M. Harsha, S. Sengupta, Effect of porosity of conducting matrix on a phase change energy storage device, International Journal of Heat and Mass Transfer, 93 (2016) 9-16.

[43] A.A. Al-Abidi, S. Mat, K. Sopian, M.Y. Sulaiman, A.T. Mohammad, Numerical study of PCM solidification in a triplex tube heat exchanger with internal and external fins, International Journal of Heat and Mass Transfer, 61 (2013) 684-695.

[44] Myers Petrochemical Co., Ltd., the price of paraffin, https://www.912688.com/supply/374994405.html, Souhaohuo, Jingmen,

[45] Wanfu Co., Ltd., the price of basalt, https://www.shashiyi.cn/sell/show-558.html, SHASHIYI, Hangzhou, 2022.

[46] Xingzi Rongxing Stone Co., Ltd., the price of granite, https://www.shashiyi.cn/sell/show-489.html, SHASHIYI, Jiujiang, 2023.

[47] Tangshan Stone Co., Ltd., the price of gneiss, https://www.kjzj.com/info/sandprice17790.html, Kuangjizhijia, Tianjin, 2022.

[48] Xuanguang Mineral Co., Ltd., the price of marble, https://site.china.cn/shashi1/4269482336.html, SiteChina, Shijiazhuang, 2022.

[49] Tianhao Mineral Co., Ltd., the price of quartzite, http://goods.jc001.cn/detail/2626841.html, Jiuzheng Building Materials, Shijiazhuang, 2022.

[50] Mingqiang Stone Co., Ltd., the price of sandstone, https://www.kjzj.com/info/sandprice17790.html, Kuangjizhijia, Longyan, 2022.

[51] L.T. Terziotti, M.L. Sweet, J.T. McLeskey, Modeling seasonal solar thermal energy storage in a large urban residential building using TRNSYS 16, Energy and Buildings, 45 (2012) 28-31.